Minimum-Current-Stress Boundary Control Using Multiple-Phase-Shift based Switching Surfaces

Haochen Shi, *Student Member*, IEEE, Huiqing Wen, *Senior Member*, IEEE, Yihua Hu, *Senior Member*, IEEE, Lin Jiang, *Senior Member*, IEEE, Zhenyan Cao

***Abstract*—The derivation and implementation multiple-phase-shift based switching surfaces for a dual active bridge (DAB) converter is the main focus of this paper. Firstly, the mathematical models of multiple natural switching surfaces (NSS) under different operation states of DAB converters are derived, which lays the foundation to achieve fast transient response during start-up, sudden voltage reference and load changing conditions. Moreover, in order to improve the overall performance of DAB converters systematically, a minimum-current-stress boundary control (MBC) is proposed that can reduce inductor peak current stress and achieve fast dynamic response simultaneously by using the multiple-phase-shift based switching surfaces. The analytical derivation of the proposed MBC is presented together with simulation and experimental evaluations, which shows the superior performance of the proposed MBC algorithm in terms of the efficiency and dynamic response improvement under various operating conditions.**

***Index Terms*—Boundary Control, Current Stress, Dual Active Bridge Converter, Dynamic Response, High Frequency Link Analysis.**

NOMENCLATURE

V_1	Primary voltage magnitude of the DAB converter
v_2	Secondary voltage magnitude of the DAB converter
C_2	Output capacitor
L_s	Leakage inductor
k	Voltage conversion ratio
u_1	State coefficient of primary voltage
u_2	State coefficient of secondary voltage
$\lambda_{(1\text{-}16)}$	Trajectory of natural switching surface
$i_{L\_\lambda x}$	Current reference of natural switching surface
D_1	Equivalent primary inner phase-shift
D_2	Equivalent secondary inner phase-shift
D_3	Equivalent outer phase-shift
T	Normalized transmission power
I_{PK}	Normalized current stress
T_0	Demanded transmission power

I. INTRODUCTION

As one of the key components in the power transmission system, the isolated bidirectional DC-DC converter is acting as the power interface for accommodating different voltage levels among various power generators, energy storage devices and power semiconductor devices. The dual active bridge (DAB) DC-DC converter is widely regarded as one of the most popular topologies due to the advantages of good power isolation, high power density, bidirectional power flow, and wide voltage conversion range. Thus, recently DAB converters have been commonly used in renewable energy power stations, Micro-grids, and Electric Vehicles [1-5].

The most commonly adopted control strategy of DAB converters is the single-phase-shift (SPS) control, which is applied a fixed 50% duty cycle PWM waveform for each switch and controlled the phase shift between the primary and secondary bridge. However, the traditional SPS control may result in large backflow current, low control flexibility and narrow soft switching range [6].

To address these problems, many advanced multiple-phase-shift (MPS) controls combined with MPS-based optimization strategies have been discussed by introducing additional phase shift variables [7-9]. One of the popular MPS strategies is the extend phase shift (EPS) control, which is effective in reducing the backflow power and extending the soft switching region by adding one additional phase shift within the high voltage bridge of DAB converters [7]. Based on the EPS control, a minimum-reactive-power oriented optimization algorithm is proposed in [8] to reduce the reactive power and achieve high transmission efficiency of DAB converter under various load and voltage conversion conditions. Besides, by building a detailed losses model including the conduction and switching losses, an EPS-based minimum-conduction-losses algorithm is proposed, which significantly improves the transmission efficiency of the DAB converter [9]. Another popular MPS control is the triple phase shift (TPS) control, which will further improve the overall performance of the DAB converter by adding two additional phase shift variables. Based on the TPS control, a minimum-current-stress based algorithm is proposed to improve the transmission efficiency of the DAB converter, especially for light load and high conversion ratio conditions [10]. Besides, the root-mean-square value of the inductor current is modeled and taken as the main optimization objective in order to reduce the conduction loss and achieve high efficiency [11]. However, these optimization strategies are only focused on the steady-state without considering the dynamic performance improvement. Furthermore, these steady-state optimizations are based on the piecewise time-domain model, which results in a complicated and cumbersome optimization process.

In order to achieve an optimum and robust dynamic response, many research efforts have been made such as feedforward compensation [12], bandstop filter and feedforward control [13], and additional proportional-resonant control [14]. However, all these strategies assume a small signal excitation around a steady-state operating point, which may ignore some important large-signal dynamic aspects. The effectiveness of these small-signal based strategies is limited within a small area in the vicinity of the operating point, which is unsuitable for the analysis of large disturbances in the input voltage or load. Moreover, these methods are based on the proportional integral (PI) controller, which have some inherent limitations such as the tradeoff between robustness and transient response, which is hard to achieve simultaneously [15]. The PI parameters are highly dependent on the specific operating conditions, which are hard to ensure high robustness under uncertain operation conditions such as variation of input/output voltage and load condition [16]. Therefore, some advanced nonlinear control such as the sliding mode control is presented in [17], which can enhance dynamic performance and achieve better robustness than the traditional PI-based

controls. However, the expense of the sliding mode control is the transformer DC bias current and increased transient period during output voltage and load changing conditions [18]. Although several fast-transient methods have been presented in [19-21] for eliminating DC bias current and reducing the transient time of DAB converters, however, these methods are mainly targeted on the load changing condition. Furthermore, the dynamic response performance of these strategies needs to be further optimized.

The boundary control algorithm using natural switching surface (NSS) was successfully implemented in the control of DC-DC converters [22-24], which can significantly improve transient response speed while reducing bias voltage during reference and load change condition by allowing all switching actions happened on their natural switching surfaces. However, those strategies are originated from the SPS control, which has limited switching states and is unable to improve the dynamic and steady-state performance simultaneously. In order to further exploit the potential of boundary control for DAB converters, a boundary control with six natural switching surfaces is proposed in [25], which adopts burst mode and SPS mode to improve the conversion efficiency for the light load and medium load conditions, respectively. However, a general control scheme for MPS-based boundary control is highly demanded, which shows the best balance for the steady-state and different dynamic transients.

In this paper, a minimum-current-stress boundary control (MBC) by using the multiple-phase-shift based switching surfaces is proposed. Firstly, the operation principle and the mathematic model of the boundary control with multiple natural switching surfaces are proposed. The current stress minimization for the steady state can be achieved by the Lagrange multiplier optimization method. Then, the complete MBC algorithm implementation flowchart is given. After that, both simulation and the experimental results are provided to validate the effectiveness of the proposed MBC algorithm, which that can reduce current stress and achieve fast dynamic response simultaneously for different load conditions such as the start-up process, sudden voltage reference and load changing conditions.

II. Normalized Derivation

Fig. 1 shows the topology of DAB converter, which consists of a symmetrical primary full bridge H_1 and secondary full bridge H_2 connected via a high-frequency transformer. Because the magnetizing inductance of the transformer is considerably larger than the leakage inductance L_S, the magnetizing inductance can be ignored in the following analysis. In Fig.1, n represents the turns ratio of the transformer. v_{h1} and nv_{h2} represent the square-wave AC voltages, which are converted by the full bridge converter in each bridge from the input voltage V_1 and output voltage v_2, respectively. Then, the difference of v_{h1} and nv_{h2} are applied on the leakage inductance to generate a piecewise-linear changing inductor current i_L. In this paper, we assume V_1 is always larger than equivalent output voltage nv_2. Due to the symmetrical structure, similar analysis can be made for the condition of "V_1<nv_2".

Considering the possible values of v_{h1} and v_{h2} under different switching states, u_1 and u_2 are used to define the relationship of AC voltage with their corresponding dc terminal voltage as:

$$v_{h1} = u_1 V_1, \quad nv_{h2} = nu_2 v_2 \tag{1}$$

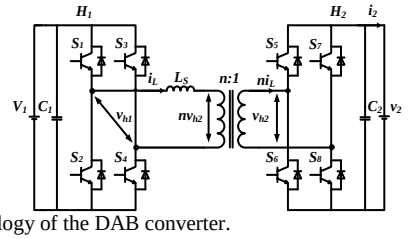

Fig.1 Topology of the DAB converter.

According to the DAB operation states analysis in [10], the DAB converter with a general TPS control can be divided into different natural switching states (NSS) with different values for AC voltage pair [v_{h1}, v_{h2}]: [V_1, -n_{v2}], [V_1, 0], [V_1, n_{v2}], [0, n_{v2}], [-V_1, n_{v2}], [-V_1, 0], [-V_1, -n_{v2}], [0, -n_{v2}] and [0, 0] states. Because there are two switching conditions for v_{h1}=0 or v_{h2}=0 situation, each AC voltage pair [V_1, 0], [0, n_{v2}], [-V_1, 0], [0, -n_{v2}] has two natural switching surfaces. At the same time, [0, 0] has four different combinations of NSS. Thus, there are totally 16 operation states by using TPS control. Taking the inductor current and output voltage as the state variables, 16 possible natural switching surfaces λ_1 to λ_{16} can be defined to describe the relationships between the inductor current i_L and output voltage v_2 under different switching states. Table I lists the complete switching states with their state coefficients [u_1,u_2] under different switching surfaces λ_1 to λ_{16}, where "1" and "0" represent the on and off state, respectively. As shown in Table I, the gate signals of S_1~S_8 under each natural switching surface can be determined. Furthermore, each switching surface contains its state coefficient and the switching sequence.

Although TPS control has multiple operation modes, considering the characteristics of each mode and the mapping relationships among different modes, two modes, namely **Mode I** and **Mode II** as shown in Fig. 2 and Fig. 3, is capable of providing the full power range and the optimal performance in terms of the inductor *RMS* current and the conduction losses [26]. Therefore, 10 natural switching surfaces from λ_1 to λ_{10} for **Mode I** and **Mode II** are selected for detailed analysis and performance optimization.

TABLE I
COMPLETE NSS WITH THEIR STATE COEFFICIENTS AND SWITCHING SEQUENCES

NSS	u_1	u_2	S_1	S_2	S_3	S_4	S_5	S_6	S_7	S_8
λ_1	1	-1	1	0	0	1	0	1	1	0
λ_2	1	0	1	0	0	1	1	0	1	0
λ_3	1	1	1	0	0	1	1	0	0	1
λ_4	0	1	0	1	0	1	1	0	0	1
λ_5	-1	1	0	1	1	0	1	0	0	1
λ_6	-1	0	0	1	1	0	0	1	0	1
λ_7	-1	-1	0	1	1	0	0	1	1	0
λ_8	0	-1	1	0	1	0	0	1	1	0
λ_9	0	0	0	1	0	1	0	1	0	1
λ_{10}	0	0	1	0	1	0	1	0	1	0
λ_{11}	1	0	1	0	0	1	0	1	0	1
λ_{12}	-1	0	0	1	1	0	1	0	1	0
λ_{13}	0	1	1	0	1	0	1	0	0	1
λ_{14}	0	-1	0	1	0	1	0	1	1	0
λ_{15}	0	0	0	1	0	1	1	0	1	0
λ_{16}	0	0	1	0	1	0	0	1	0	1

In order to build a general mathematic model of natural surface trajectory λ_1 to λ_{10}, the differential equations of the relationship between the inductor current and output voltage under the various NSS are analyzed. Firstly, the normalized equations can be used to simplify the expressions:

$$V_{1n}=\frac{V_1}{V_{ref}},\ v_{2n}=\frac{v_2}{V_{ref}},\ i_{Ln}=\frac{i_L Z_0}{V_{ref}},\ i_{2n}=\frac{i_2 Z_0}{V_{ref}},\ t_n=tf_0 \tag{2}$$

where V_{ref} is the reference voltage of the output voltage, Z_0 represents the base impedance $Z_0=\sqrt{L/C}$ and f_0 represents the natural frequency $f_0=1/(2\pi\sqrt{L/C})$. The L and C is the inductance of leakage inductance L_s and the capacitance of output capacitor C_2.

Based on the operation principle of DAB converter and normalized equation in (2), the normalized differential equations for output voltage v_{2n} and inductor current i_{Ln} can be derived as:

$$\begin{aligned} dv_{2n}/dt_n &= 2\pi\left(ni_{Ln}u_2-i_{2n}\right)\\ di_{Ln}/dt_n &= 2\pi\left(V_{1n}u_1-nv_{2n}u_2\right)\end{aligned} \tag{3}$$

According to equation (3), the transient state of output voltage v_2 is determined by inductor current i_L while the normalized inductor current i_{Ln} can be calculated by the voltage difference between unified primary bridge voltage $V_{1n}u_1$ and secondary bridge voltage $nv_{2n}u_2$.

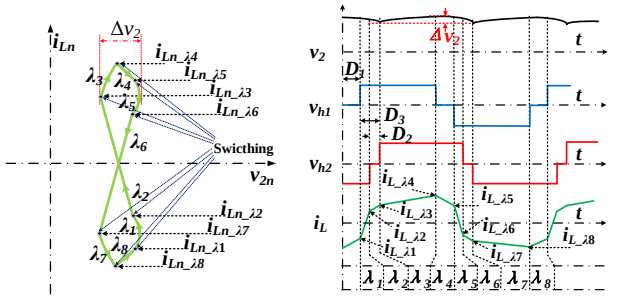

Fig.2. Steady state operation of Mode I: (a) Trajectories shown in the phase plane of i_{Ln} versus v_{2n}. (b)Typical time-domain waveforms.

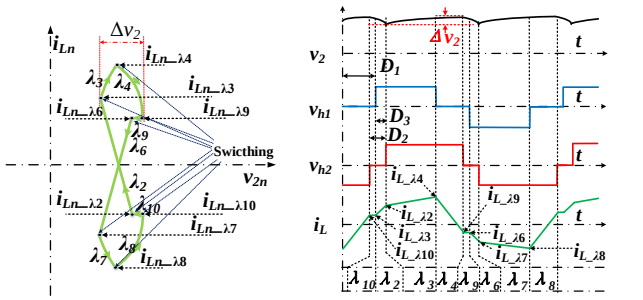

Fig.3. Steady state operation of Mode II: (a) Trajectories shown in the phase plane of i_{Ln} versus v_{2n}. (b) Typical time-domain waveforms.

When the secondary state coefficient u_2 is nonzero, the second-order differential equation based on (3) is:

$$\begin{aligned} d^2i_{Ln}/dt_n^2 &= 4\pi^2nu_2\left(i_{2n}-ni_{Ln}u_2\right)\\ d^2v_{2n}/dt_n^2 &= 4\pi^2nu_2\left(V_{1n}u_1-niv_{2n}u_2\right)\end{aligned} \tag{4}$$

By determining the characteristic root of the second order differential equation shown in (4), a general solution for the second order differential equation can be derived as:

$$\begin{aligned} i_{Ln} &= \left(i_{Ln}(t_{0n})-i_{2n}u_2/n\right)\cos(2\pi nt_n)+\left(-u_2v_{2n}(t_{0n})+V_{1n}u_1/n\right)\sin(2\pi nt_n)+i_{2n}u_2/n\\ v_{2n} &= \left(v_{2n}(t_{0n})-V_{1n}u_1/nu_2\right)\cos(2\pi nt_n)+\left(i_{Ln}(t_{0n})/u_2-i_{2n}/n\right)\sin(2\pi nt_n)+V_{1n}u_1/u_2n\end{aligned} \tag{5}$$

where $i_{Ln}(t_{0n})$ and $v_{2n}(t_{0n})$ represent the initial value of normalized inductor current and output voltage. The sinusoidal and cosinoidal terms in (5) are deriving from the general solution of the second order differential equation, which indicates the change rule of the inductor current in the time-varying resonant network. The equation (5) matches the analysis in [22] and [23], which validates that the state variables in the second order differential equation, including i_{Ln} and v_{2n}, contain both the sinusoidal and cosinoidal terms. In order to regulate the switching frequency and the output voltage during the steady state, the normalized inductor current reference $i_{Ln\_\lambda x}$ is introduced [25]. Then, a unified initial inductor current $i_{Ln}(t_{0n})$ and output voltage $v_{2n}(t_{0n})$ can be expressed by:

$$v_{2n}(t_{0n})=1, i_{Ln}(t_{0n})=i_{Ln\_\lambda x}u_2 \tag{6}$$

Combining equations (4)-(6), mathematic expression of the following six NSS trajectories can be expressed as:

$$\begin{aligned}\lambda_{(1,3,4,5,7,8)} &= (v_{2n}-V_1u_1u_2/n)^2-(i_{Ln\_\lambda x}-i_{2n}u_2/n)^2-\\ &\quad (V_{1n}u_1/n-u_2)^2+(i_{Ln}-i_{2n}u_2/n)^2\end{aligned} \tag{7}$$

where $i_{Ln\_\lambda x}$ is the inductor current reference under different operation states during the steady-state. $i_{Ln\_\lambda x}$ is used to maintain the operational frequency of the DAB converter as the desired frequency, which will be discussed with details in the following section.

Once the secondary state coefficient is zero, namely "u_2=0", the state function in (3) can be simplified as:

$$\begin{aligned} dv_{2n}/dt_n &= -2\pi i_{2n}\\ di_{Ln}/dt_n &= 2\pi V_{1n}u_1\end{aligned} \tag{8}$$

The solution of (8) can be expressed as:

$$\begin{aligned} v_{2n} &= -2\pi i_{2n}t_n+v_{2n}(t_{0n})\\ i_{Ln} &= 2\pi V_{1n}u_1t_n+i_{Ln}(t_{0n})\end{aligned} \tag{9}$$

Based on (9), it is clear that the inductor current i_L and output voltage v_2 is decoupled when u_2 is equal to 0. Then, the trajectories for the following four NSS trajectories can be expressed as:

$$\lambda_{(2,6,9,10)}=i_{Ln}-i_{Ln\_\lambda x}+\frac{V_{1n}u_1v_{2n}}{i_{2n}}-\frac{V_{1n}u_1v_{2n}}{i_{2n}} \tag{10}$$

where i_L and v_{2n} show the linear relationship, which make the four NSS trajectories become straight line instead of circle.

III. NSS Trajectories

Considering that there are total 10 possible NSS trajectories for the normal operation of DAB converter [10], two operation modes are divided for the boundary control: **Mode I** and **Mode II** shown in Fig. 2(a) and Fig. 2(b), respectively. In Fig. 2, trajectories λ_1-λ_{10} are natural switching surfaces of DAB converter and the arrow is used to show the operation direction of each trajectory.

For the steady-state condition of **Mode I** in Fig.4(a), the NSS trajectories λ_1-λ_8 are adopted and DAB converter is naturally switching to next operation states at the intersections of trajectories. All switching actions are arranged around the reference voltage, which ensures the output voltage can be maintained as the desired value. Trajectories of **Mode II** are illustrated in Fig.4(b), which shows that the switching sequence is set as λ_2-λ_3-λ_4-λ_9-λ_6-λ_7-λ_8-λ_{10}. Specially, trajectories λ_2, λ_6, λ_9, λ_{10} are straight lines that are followed (10).

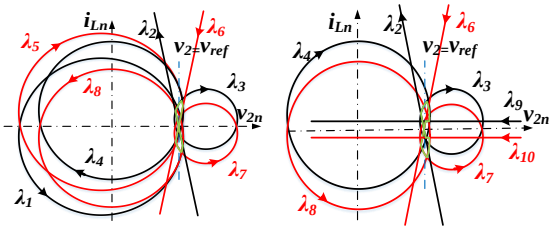

(a) (b)

Fig. 4. Natrual switching surfacer of DAB converter (a) Mode I. (b) Mode II.

A detailed steady-state operation of the DAB converter under the phase plane of i_{Ln} versus v_{2n} is shown in Fig. 3(a). The switching sequence of the NSS trajectories is set as λ_1-λ_2-λ_3-λ_4-λ_5-λ_6-λ_7-λ_8-λ_1, the operation trajectory during one cycle is symmetrically distributed with respect to v_{2n} axis. Thus, the average output voltage is maintained as constant during one switching cycle while the normalized inductor current i_{Ln} exhibits axial symmetry, which avoids the transformer dc-bias current. It shows all switching actions are conducted at the designed inductor current reference $i_{Ln\_\lambda x}$, while the voltage variation in the steady state Δv_2 is clearly illustrated to check with the design specification. Fig. 3(b) show the corresponding waveforms of primary voltage v_{h1}, secondary voltage v_{h2}, inductor current i_L and output voltage v_2. It can be seen that each NSS trajectory is in accordance with the waveform of DAB converter. For example, the trajectory λ_1 indicates that the inductor current is increasing from negative to positive while the output voltage is slightly decreasing, which is the same as Fig.3(a). Moreover, Fig. 4 indicates that all switching condition happens on inductor current reference $i_{L\_\lambda x}$, so the period of each operation trajectory can be determined with the set inductor current references.

The NSS trajectories and equivalent waveforms of the boundary control under **Mode II** are shown in Fig.4. Similar as previous analysis of **Mode I**, switching sequence λ_2-λ_3-λ_4-λ_9-λ_6-λ_7-λ_8-λ_{10}-λ_2 have occurred at related inductor current reference $i_{Ln\_\lambda x}$. The corresponding time-domain waveforms are illustrated in Fig.4(b), which prove the effectiveness of the TPS-based boundary control for the steady-setae operation.

Considering the relationship of the NSS trajectories and the time-domain waveforms, the inductor current reference $i_{Ln\_\lambda x}$ can be calculated by:

$$Mode\ I: i_{Ln\_\lambda x}=\begin{cases} i_{Ln\_\lambda 1}=-i_{Ln\_\lambda 5}=-nZ_0[k-kD_1-D_2+2D_3-1]/(4f_sL) \\ i_{Ln\_\lambda 2}=-i_{Ln\_\lambda 6}=nZ_0[kD_1-2kD_2-D_2+2kD_3+1-k]/(4f_sL) \\ i_{Ln\_\lambda 3}=-i_{Ln\_\lambda 7}=nZ_0[kD_1-D_2+2kD_3+1-k]/(4f_sL) \\ i_{Ln\_\lambda 4}=-i_{Ln\_\lambda 8}=nZ_0[2D_1-kD_1-D_2+2D_3+k-1]/(4f_sL) \end{cases} \tag{11}$$

$$Mode\ II: i_{Ln\_\lambda x}=\begin{cases} i_{Ln\_\lambda 2}=-i_{Ln\_\lambda 6}=-nZ_0[-kD_1-1+D_2+k]/(4f_sL) \\ i_{Ln\_\lambda 3}=-i_{Ln\_\lambda 7}=nZ_0[kD_1+2kD_3-D_2+1-k]/(4f_sL) \\ i_{Ln\_\lambda 4}=-i_{Ln\_\lambda 8}=nZ_0[-kD_1+2D_1-D_2+2D_3+k-1]/(4f_sL) \\ i_{Ln\_\lambda 9}=-i_{Ln\_\lambda 10}=nZ_0[-kD_1-1+D_2+k]/(4f_sL) \end{cases} \tag{12}$$

where f_s is the desired operation frequency, D_1 is the primary inner phase shift, D_2 is the secondary inner phase shift, D_3 is the outer phase shift control, and the voltage conversion ratio k is defined as: $k=V_1/nv_2$. Thus, reference inductor current $i_{Ln\_\lambda x}$ for two modes can be determined according to (11) and (12), respectively.

IV. Proposed MBC Algorithm

This section will discuss the derivation and operation principle of the minimum-current-stress boundary control (MBC), which covers the multiple-natural-switching surfaces (NSS) boundary control based dynamic improvement and the minimum-current-stress oriented steady state optimization.

A. Dynamics Based on the NSS Boundary Control

Because the boundary control can regulate different natural switching surfaces directly, it can ensure fast dynamic response by controlling the intersection of different NSS trajectories and the target operating point. Fig. 5 illustrates the trajectory by using the TPS-based boundary control from an initial operation point B to the steady-state operation condition. During the dynamic process of boundary control, the direction of each NSS is fixed, while the radius of each trajectory can increase or decrease with respect to the of initial output voltage $v_{2n}(t_{0n})$ and initial inductor current $i_{Ln}(t_{0n})$. From point B to reach steady-state condition, it can follow trajectories λ_3 *or* λ_5, which is forced operation condition to get close to steady-state λ_1. After it reaches steady-state trajectory λ_1, it can follow as the steady-state operation shown in Fig. 2(a).

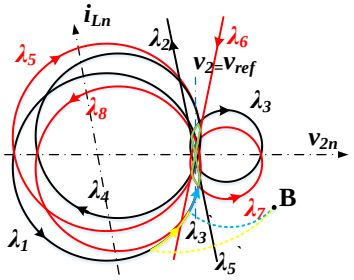

Fig. 5. Concept dynamic trajectories from point B to the steady-state.

The start process of DAB converter under **Mode I** is illustrated in Fig. 6(a). The initial condition of DAB converter is v_{2n}=0 and i_{Ln}=0 at point T_1. Then, with the boundary control, the trajectory λ_1 with u_1=1 and u_2=-1 is adopted to guide the operation point from T_1 to T_2, which is the intersection of trajectory λ_1 and λ_2. After that, trajectory λ_2 with u_1=1 and u_2=0 is applied until reach the T_3. During the switching surface λ_1 and λ_2 from T_1 to T_3, the inductor current i_L is rapid growing while the normalized output voltage v_{2n} is still maintained close to 0. After reaching T_3, the operation state is switching to λ_3 with u_1=1 and u_2=1 state. Both of i_L and v_2 are increasing during λ_2 surface before it reaches point T_4. After that, the operation surface will switch from trajectory λ_3 to trajectory λ_4 with u_1=0 and u_2=1 until it reaches the steady-state at point T_5. It is clear that boundary control can accomplish the entire start-up stage by switching the operation trajectory from λ_1–λ_2–λ_3–λ_4, which can significantly reduce the start-up duration.

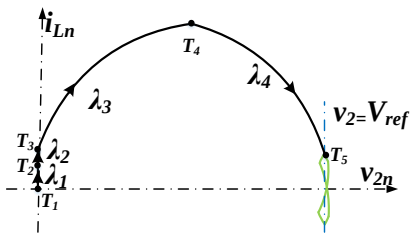

(a)

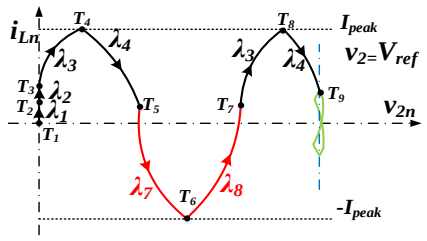

(b)

Fig. 6. Start-up process by using the boundary control (a) without maximum inductor current limitation. (b) with maximum inductor current limitation I_{peak}.

However, the amplitude of inductor current i_L during the start-up process is much larger than that during the steady-state, which may damage the semiconductor device and cause saturation of magnetic components. For safe operation of DAB converter, the maximum inductor current limitation needs to be limited with the boundary control law [23]. The start-up stage operation of DAB converter with the set maximum inductor current limitation "$\pm I_{peak}$" is shown in Fig.4(a). It can be seen that the NSS trajectory of the DAB converter is forced to switch from λ_3 to λ_4 when the inductor current is reached the I_{peak}. After reaching point T_5, λ_7 is used until the inductor current is equaled to negative current limitation "$-I_{peak}$". Then, the transient operation state will switch to λ_8 until reach point T_7. Overall, it can be seen that the switch sequence of boundary control with maximum inductor current limitation is cycling among λ_3-λ_4-λ_7- λ_8. Then, the inductor current is periodically changing between inductor current limitation $\pm I_{peak}$ while the output voltage v_2 is always increased until it reaches the reference voltage V_{ref} and transferred into steady-state operation at point T_9. Although the adoption of maximum inductor current limitation causes more switching actions and long transient time to reach the steady-state operation, the possible overcurrent fault on semiconductor devices and the saturation of magnetic components are effectively avoided.

B. Minimum-Current-Stress Steady-State Optimization

Considering three phase-shift variables (D_1, D_2, D_3) in the TPS, the duration of trajectories λ_1-λ_{10} can be accurately controlled by adjusting the value of D_1, D_2 and D_3. Although there are infinite combinations of D_1, D_2 and D_3 for given load and voltage conversion conditions, an optimal combination of phase-shift variables (D_1, D_2, D_3) can be obtained by setting a specific optimization objective to improve the overall efficiency of the DAB converter.

For obtaining an optimal phase-shift combination of DAB converters under TPS control, the mathematical expression of the transmission power for two different modes needs to be established. The corresponding expressions for two modes can be written as:

$$Mode\ I: T=\frac{P}{P_N}=\begin{bmatrix}2D_3^2-D_1^2-D_2^2+2D_3+D_1-D_2\\+D_1D_2+2D_2D_3-2D_1D_3\end{bmatrix} \tag{13}$$

$$Mode\ II: T=\frac{P}{P_N}=[D_1-D_2+2D_3+D_1D_2-2D_1D_3-D_1^2-D_3^2] \tag{14}$$

where the normalized power is expressed by "$P_N=V_1*nv_2/(8f_s*L)$", the voltage conversion ratio is "$k=V_1/nv_2$", and f_s is the desired switching frequency. Besides, the variation range of variable D_1, D_2 and D_3 is set from 0 to 1.

Then, the inductor peak current stress, which can reflect the root mean square (RMS) value of inductor current and determine the conduction losses of DAB converter, is adopted as the optimization objective function. Specifically, in order to improve the overall transmission efficiency of DAB converters, the minimum current stress should be achieved for a given transmission power. Thus, the inductor peak current for both **Mode I** and **Mode II** can be expressed as:

$$I_{pk}=i_{Ln\_\lambda 4}=\frac{nZ_0}{4f_sL}[-kD_1+2D_1-D_2+2D_3+k-1] \tag{15}$$

According to (13)–(15), the optimal minimum current stress algorithm can be calculated by Lagrange multiplier method (LMM), which is expressed by:

$$L=M+\mu(T-T_0) \tag{16}$$

where L is the Lagrangian function, μ is the Lagrangian multiplier and T_0 is the demanded transmission power. The Lagrangian function L can be solved by following restricted conditions as:

$$\begin{cases}\dfrac{\partial L}{\partial D_1}=0,\dfrac{\partial L}{\partial D_2}=0,\dfrac{\partial L}{\partial D_3}=0\end{cases} \tag{17}$$

By applying constraints in (16) into Lagrangian function in (17), the solution of LLM can be expressed as:

$$Mode2:\begin{cases}D_1=1-\sqrt{\dfrac{T_0}{2(k-1)}}\\D_2=1-k(1-D_1)\\D_3=0\\T\in\left[0,\ 2\dfrac{k-1}{k^2}\right]\end{cases}\ Mode1:\begin{cases}D_1=(k-1)\sqrt{\dfrac{1-T_0}{k^2-2k+2}}\\D_2=0\\D_3=\dfrac{k-kD_1-1}{2k-2}\\T\in\left[2\dfrac{k-1}{k^2},\ 1\right]\end{cases} \tag{18}$$

Based on the optimization algorithm in (18), the inner phase shift D_1 is determined by the voltage conversion ratio k and the demanded transmission power T_0. Then, the other phase shifts D_2 and D_3 can be directly calculated from D_1. Thus, for each T_0 and k, the optimum phase shift combination (D_1, D_2, D_3) can be derived. In particular, the optimal TPS control will be evolved into the triangular modulation and EPS modulation under the light-load and heavy-load conditions [10, 27].

Based on the above analysis, a minimum-current-stress boundary control (MBC) can be proposed. Two mechanisms mainly determine the operation principle of the MBC algorithm: one is the natural switching surface boundary control for achieving fast dynamic respond and the other is the minimum current stress optimization for ensuring the lowest inductor current stress operation during the steady state operation. In the implementation of the proposed MBC, the first step is to determine the optimal phase shifts D_1, D_2 and D_3 for the output voltage reference v_{ref} and the demanded transmission power T_0 with the optimization target of the minimum current stress shown in (15). After that, the inductor current reference $i_{Ln\_\lambda x}$ can be calculated according to the expressions in (11) and (12). Then, the MPS-based NSS boundary control is implemented based on the intersection of the different NSS trajectories and the target operating point. The inherent mechanism of the proposed MBC can enhance the dynamic and steady performance of DAB converters simultaneously. Besides, it can avoid steady state error by slightly adjusting operation frequency, when the system parameters are deviated from the estimated values.

C. Complete MBC Algorithm

Through the online calculation of the phase-shift variables in TPS control, the proposed minimum-current-stress boundary control (MBC) algorithm is implemented by using the finite

state machine without PI control, which is different from the traditional closed-loop control which is relied on the PI controller. The flowchart of the proposed MBC control is illustrated in Fig.7. Firstly, the voltage and current sensors are used to measure the input voltage V_1, output voltage v_2 and output current i_2 as well as the inductor current i_L. Then, the voltage conversion ratio k and normalized unified power T can be calculated by these measurements and reference voltage V_{ref}. On this basis, the optimized phase shift D_1, D_2 and D_3 can be determined through the equation (19), while the corresponding inductor current reference $i_{L\_\lambda x}$ is calculated by (11) for **Mode I** or (12) for **Mode II**. Two main criteria are adopted to judge whether the trajectory switching actions are implemented or not: one is the corresponding trajectory is negative and the other is whether the measured current is larger than the set limit when the maximum inductor current protection is adopted. For instance, as illustrated in Fig.7, the MBC control will switch to the switching surface λ_2 from λ_1 when the operating point is reaching the intersection between λ_1 and λ_2, which is the $\lambda_2 \geq 0$ condition. Otherwise, the previous trajectory λ_1 will be maintained. Once the set current limitation is achieved, the switching action is demanded. For instance, with the buck operation, the current limitation is achieved in switching sequence from λ_3 and λ_4 due to the maximum inductor current is occurred at the end of λ_3. The inductor current i_L will firstly compare with the set maximum inductor current limitation I_{peak}. If the inductor current i_L is exceeded the I_{peak}, the proposed MBC control will force DAB converter switch to the trajectory λ_4. Similarly, the maximum inductor current limitation on the negative current period is achieved by adding additional constraint "i_L<-I_{peak}" between λ_6 and λ_7. Finally, when trajectory λ_8, the two criteria will be used to determine if the next trajectory λ_1 will be implemented or not. Besides, when the system parameters are found significantly deviated from the rated value, the switching frequency is slightly changed in order to accommodate the parameter variations.

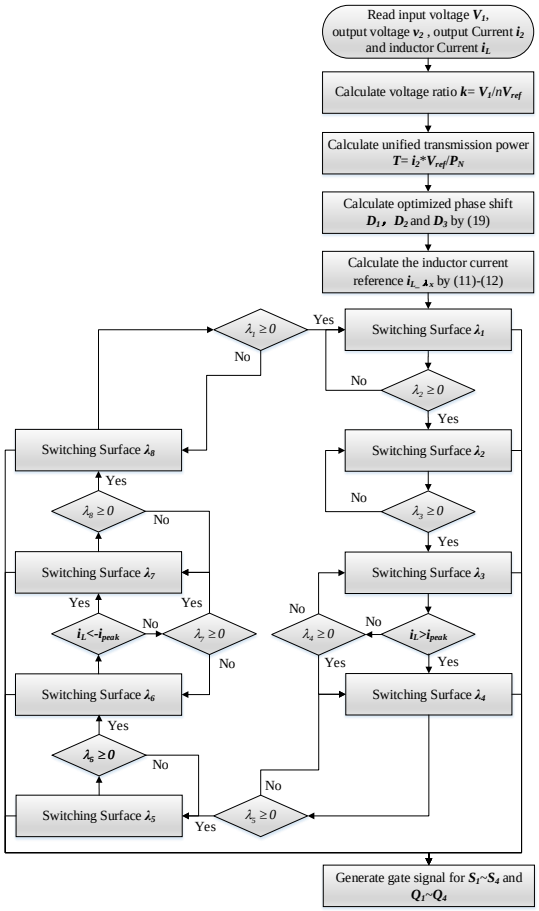

Fig. 7. Flowchart of the proposed MBC algorithm.

D.Theoretical Evaluation

Fig. 8 (a) shows the theoretical comparison results among SPS, two EPS controls (EPS1, EPS2), and MBC control when voltage conversion ratio k=2. The difference of EPS1 and EPS2 lies on the value for D_1. Specifically, D_1=0.25 is used for EPS1 while D_1=0.33 is used for EPS2. It can be seen that the normalized RMS current values by using EPS1 and EPS2 are lower than SPS control, but the maximum transmission powers by using EPS1 and EPS2 are found less than that of SPS control. Compared with EPS1, EPS2 has lower RMS current and narrower transmission power range. It indicates that the inner phase shift D_1 has a positive influence on the reduction of the RMS current. Besides, D_1 has a negative influence on the maximum transmission power. Among all control methods, MBC control can ensure the lowest RMS current and the largest power transmission under all load conditions.

Fig. 8(b) shows the theoretical comparison of the RMS current versus the transmission power when k=3 and k=4. Both SPS, EPS, and MBC have higher RMS current for larger voltage conversion conditions, while MBC can achieve the lowest RMS current under any voltage-conversion-ratio conditions. Therefore, it proves the MBC can ensure the lowest current stress for the steady-state operation among these strategies under all transmission power and voltage-conversion-ratio conditions.

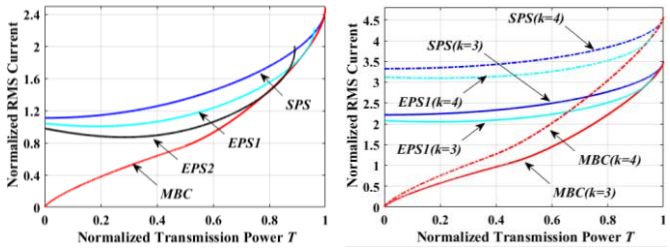

(a) (b)

Fig. 8. (a) Normalized RMS current versus normalized transmission power T by using different control methods when k=2. (b) Normalized RMS current versus normalized transmission power T and voltage conversion ratio k by using different control methods.

V. Simulation Results

In order to verify the theoretical analysis of MBC control, main simulation waveforms of the output voltage v_2, output current i_2, primary AC square wave v_{h1}, secondary AC square wave v_{h2}, and inductor current i_L under MBC control during starting up condition are shown in Fig. 9. Fig.9 (a) shows the results with 15A maximum inductor current limitation. It is shown that the proposed MBC control can handle start-up by automatically adjusting the switching sequence among multiple NSS trajectories under the constraints of the set maximum inductor current limit and the desired output voltage with a rapid transient speed. When the output voltage is moving close to the voltage reference at 50V, the MBC control is moving into the steady-state. The simulation shows that it requires 0.3ms to finish the start-up process and reach the steady-state operation. The phase plane results shown in Fig. 9(b) indicate that MBC with 15A limit takes several operation trajectories with a maximum 15A inductor current before reaching the steady-state operation.

As illustrated in Fig. 9(b), the inductor current is rapidly increasing while v_{2n} is slightly increasing during the first operation stage. Then, the output voltage is rising with the decrease of the inductor current until it reaches nearly 0. Since the output voltage is still far away from the reference voltage, it will be turning into the negative inductor current operation stage. It needs two full positive and negative operation cycles to reach the steady-state operation. Furthermore, the simulation results of the dynamic response and steady-state operation during the start-up verify the above theoretical analysis. Fig. 9(c) illustrates the results in the time domain by using the MBC control with 20A current limitation. It can be seen that the inductor current is changing within the maximum 20A current limitation during the start-up stage and the current will finally stabilize when v_2 is stable as 50V. Furthermore, it only takes two natural switching actions to reach the steady-state operation instead of multiple switching sequence cycles when 20A maximum current limitation is used. Fig. 9(b) is the results of i_{Ln} versus v_{2n} in the phase plane. It is clear that the v_{2n} is only taking a natural switching surface λ_1- λ_4 to finally settle at the steady state, which is identical with the theoretical analysis in Fig. 2(a). Compared with 15A limitation condition, the 20A condition can achieve the steady-state within 0.2ms, which is less than that of 15A limitation condition. It indicates that a larger maximum current limitation can ensure better dynamic performance and less transient time. However, a larger peak inductor current causing higher current stress on circuit components like MOSFET and transformer. Therefore, a proper maximum inductor current limitation should be set in MBC control by balancing the transient response speed and the safety issues of DAB converters.

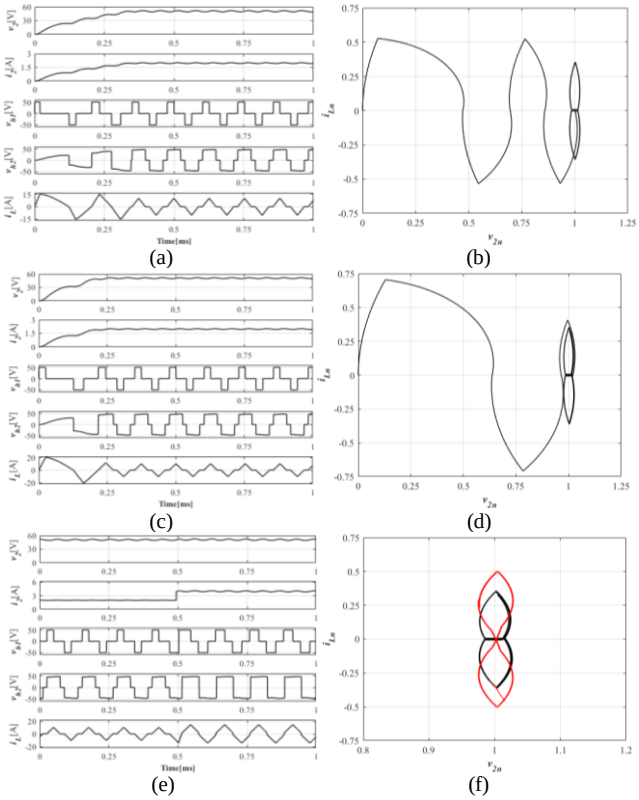

(a) (b) (c) (d) (e) (f)

Fig. 9. Simulation results of DAB converter by using the MBC control when V_1=80 V and v_2= 50 V. (a) Waveforms of the start-up stage with current limitation of 15A. (b) The phase plane of i_{Ln} versus v_{2n} when current limitation is 10A. (c) Waveforms of the start-up stage with the current limitation of 20A. (d) The phase plane of i_{Ln} versus v_{2n} when current limitation is 20A. (e) Waveforms of voltage variation condition when transmission power P is changing from 97W to 195W. (f) The phase plane of i_{Ln} versus v_{2n} under the load variation condition.

Fig.9 (e) and (f) illustrate the simulation results for the load variation conditions by using the MBC control. During time interval between 0ms and 0.5ms, the resistance of the load resistor is equal to 25.6Ω, which indicates that the transmission power in this load condition is equal to 97W. Then, the load is switching from 25.6Ω to 12.8Ω at the instant of 1ms. The corresponding power is switching from 97W to 195W. It can be seen that the output current i_2 is obviously increasing from 1.9A to 3.9A while the output voltage v_2 is always stabilized at 50V. It proves that the boundary control can achieve fast and stable dynamic response performance under load variation conditions. Furthermore, the average inductor current is always maintained as zero, which indicates MBC control can address the DC current bias problem. The phase plane results under the load variation condition are shown in Fig. 9(f), where the black line is the previous steady-state operation at 97W and the red line is the new steady-state operation at 195W. It can be seen that the previous steady state can be smoothly switched to new operation state, which proves MBC control can handle load variation conditions without the DC bias current.

VI. Experimental Results

A. Experimental prototype

The experimental prototype of the DAB converter was built to verify previous theoretical and simulation results in Fig.10. The auxiliary inductor L_s=60μH, output capacitor C_2=220μF and turns ratio of transformer n is 0.5, as well as the desired operation frequency, is f_s=8kHz. The traditional PI control and

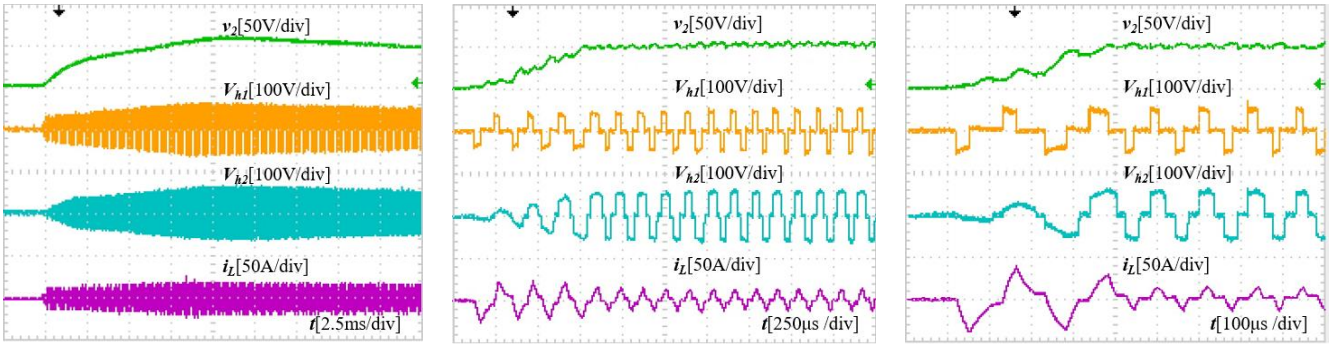

(a) (b) (c)

Fig. 11. Experimental waveforms for the start-up process of DAB converters when V_1=50V, v_2=50V and P=100W. (a) EPS control without transient optimization.(b) MBC control with 25A inductor current limitation. (b) MBC control with 40A inductor current limitation.

the proposed MBC control are implemented by programming the DSP TMS320F28335 microcontroller, and the input voltage V_1, output voltage v_2, output current i_2 and inductor current i_L are measured by voltage and current sensor which are connected to the ADC port of DSP microcontroller.

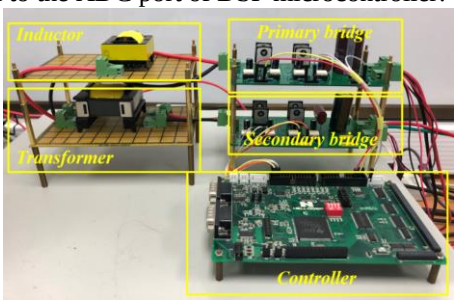

Fig. 10. Photograph of an experimental prototype

The experimental prototype of the DAB converter was built to verify previous theoretical and simulation results in Fig.10. The auxiliary inductor L_s=60μH, output capacitor C_2=220μF and turns ratio of transformer n is 0.5, as well as the desired operation frequency, is f_s=8kHz. The traditional PI control and the proposed MBC control are implemented by programming the DSP TMS320F28335 microcontroller, and the input voltage V_1, output voltage v_2, output current i_2 and inductor current i_L are measured by voltage and current sensor which are connected to the ADC port of DSP microcontroller.

B. Dynamic Response for Start-Up condition

The start-up process by using the traditional phase shift control with PI controller is shown in Fig. 11(a). Due to the limitation of the phase shift control, it can be seen that the output voltage v_2 is slowly increasing and then reaching the reference voltage 50V, which requires almost 12.5ms. In order to prevent the saturation of high frequency transformer and auxiliary inductor in a practical experiment, the start-up stage of DAB converter under MBC control will be tested with 25A and 40A maximum inductor current limitation conditions. The MBC control with 25A maximum inductor current limit is shown in Fig. 11(b), it can be seen that MBC control can significantly accelerate the start-up process by modifying the period of different operation natural surfaces. It only takes 1ms for reaching reference voltage and transferring into steady-state operation. Fig. 11(c) shows the MBC control with 40A maximum inductor current limitation, which indicates a larger maximum inductor current limitation can reduce the start-up transient time to 0.4ms. It also proves the previous simulation analysis.

C. Dynamic Response for output voltage variation condition

The experimental results by using the MBC control and EPS control under the voltage-reference change condition are shown in Fig. 12. It is clear that the EPS control needs several operational cycles to finish the output voltage change from 30V to 50V, which takes around 4ms to reach steady-state operation with v_2=50V. During this period, both the output voltage and amplitude of the secondary AC voltage v_{h2} are slowly rising within the transient period. The corresponding results by using the MBC control are shown in Fig. 12(b), which indicate that the overall transient time for changing output voltage v_2 from 30V to 50V is around 400 μs. It indicates the MBC control can achieve nearly 10 times faster dynamic performance than that with the traditional EPS control.

D. Dynamic Response for load variation condition

Fig.13 shows the comparison of the experimental results when the transmission power is changing from 125W to 250W. It can be seen that the output v_2 show slight oscillations due to the sudden change of load resistance, and then return to 50V by using the PI controller. The variation of the output voltage v_2 is small at the moment of load change. However, the output current i_2 exhibits obvious variations: firstly, it is dramatically increasing at the load-changing instant due to the reduction of load resistance. After that, the i_2 is firstly decreasing with the dropping of v_2, and then increasing with the rising of v_2. The total time for i_2 and v_2 to reach stable at 250W is around 2.25ms. Fig.13(b) shows the results by using the direct transient control [19], which regulates the phase shift variables directly at load changing moment. It shows obvious DC bias current, which may damage the semiconductor devices and saturation magnetic core of the inductor and transformer. The results by using the fast-transient control in [20] are shown in Fig.13(c). These results validate that the fast-transient control can eliminate the DC bias current and accomplish the load variation within 80μs. As illustrated in Fig. 13(d), the MBC control can achieve a fast-dynamic response within 30us, which is faster than that of the control in [20]. Furthermore, as shown in Fig. 13(d), with the proposed MBC control, no obvious DC bias current can be observed, which matches the previous simulation results in Fig.9 (e) and (f).

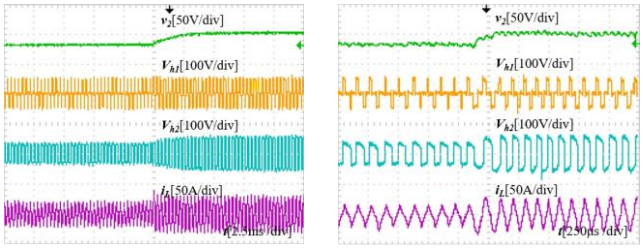

(a) (b)

Fig. 12. Experimental waveforms of DAB operation when V_1=50V and v_2 is changing from 30V to 50V (a) EPS control without transient optimization. (b) MBC control with 40A inductor current limitation.

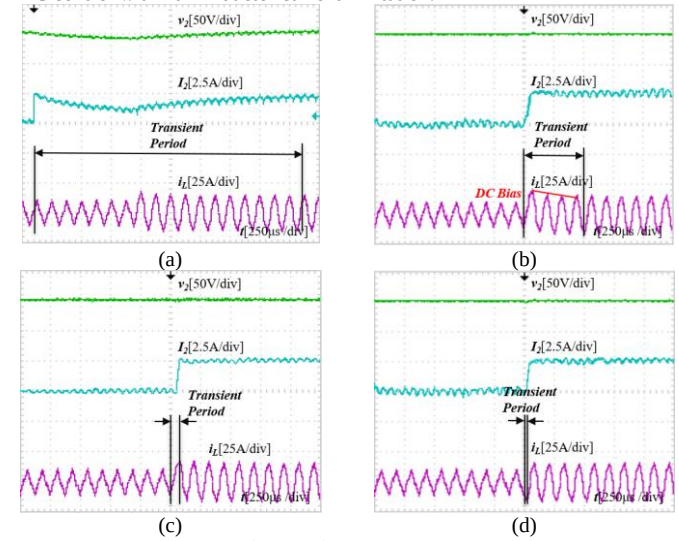

(a) (b) (c) (d)

Fig. 13. Experimental waveforms of DAB operation when V_1=50V and v_2 =50V,and transmission power is changing from 125W to 250w (a) EPS control without transient optimization; (b) Direct transient control in [19]; (c) fast-transient control in [20]; (d) proposed MBC control.

E. Steady State Optimization

Fig. 14(a) and Fig. 14(d) show experimental waveforms of SPS and MBC when k=2 and P=250W. Compared with traditional SPS control, MBC can reduce the amplitude of inductor current from 20A to 16A. The corresponding inductor rms current is decreasing from 13.5A to 10.1A, which indicates the proposed MBC control can significantly reduce current stress, which is beneficial to the reduction of conduction losses and efficiency improvement.

Fig. 14(b) and Fig.14 (e) show the experimental results for the light load condition P=125W. Due to the transmission power is lower than that under the heavy load condition, the peak of the inductor current with SPS control is 16A, which is slightly lower than that under the heavy load condition. Then, the experimental waveform of MBC control indicates that it can reduce the inductor peak current to 11.5A. The corresponding inductor rms current is decreasing from 9.3A to 6.3A, which proves the MBC can dramatically reduce current stress.

The experimental result of higher voltage conversion ratio k is shown in Fig. 14(c) and Fig.14(f). The reference voltage is changing from 50V to 30V, while the conversion ratio k is increasing from 2 to 3.34. Compared with SPS control with k=2 condition, it is clear that larger k will lead to a larger amplitude of the inductor current with the same transmission power. Thus, the negative impact of the current stress becomes more serious for larger voltage conversion situations. Fig.14(f) shows that the MBC control can reduce the inductor peak current from 22A to 14A, while the corresponding inductor rms current is decreasing from 12.5A to 8.5A Although the current stress of MBC control with larger k is also increased, it still dramatically less than SPS control, which ensures better transmission efficiency.

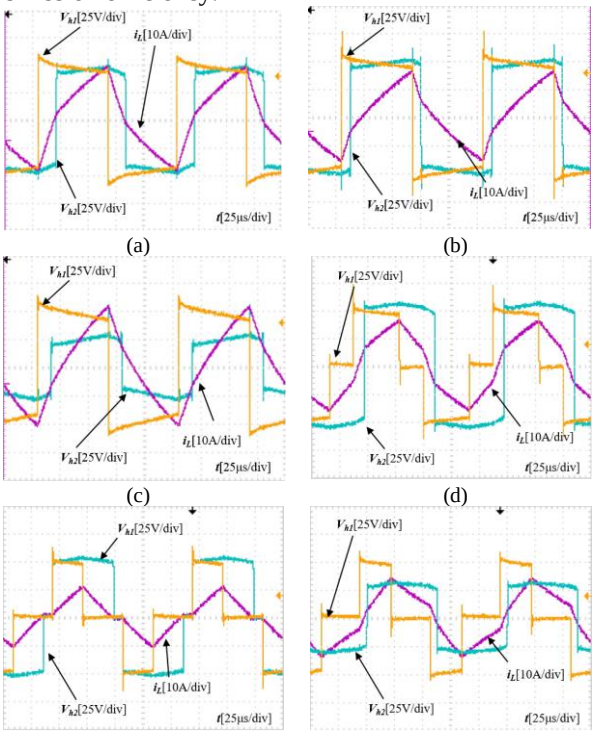

(a) (b) (c) (d) (e) (f)

Fig. 14. Experimental waveforms of DAB converter: (a)SPS control when V_1=50V, v_2=50V and P=250W. (b)SPS control when V_1=50V, v_2=50V and P=125W. (c)SPS control when V_1=50V, v_2=30V and P=125W. (d)MBC control when V_1=50V, v_2=50V and P=250W. (e)MBC control when V_1=50V, v_2=50V and P=125W. (f)MBC control when V_1=50V, v_2=30V and P=125W.

Fig. 15(a) shows the efficiency comparison of DAB converters under SPS, EPS1, EPS2, MBC, the global inductor *RMS* current modulation (GOM) proposed in [10], as well as the fundamental-optimal phase shift (FOPS) control proposed in [29]. The EPS1 is the EPS control with D_1=0.25, and the EPS2 is the EPS control with D_1=0.33. Among SPS, EPS1 and EPS2, EPS2 has better performance than SPS and EPS1 control due to larger inner phase shift D_1. However, the maximum transmission power of EPS2 becomes smaller than SPS control, which shows limited total power transmission capability. The FOPS can improve the transmission efficiency, but the overall power transmission range is limited. After that, MBC and GOM control exhibit the highest transmission efficiency especially under the light load condition among these methods, including SPS, EPS1, EPS2, FOPS, GOM and MBC control. Furthermore, MBC and GOM can achieve the same maximum transmission power as SPS control. It indicates MBC control shows obvious advantages in terms of the efficiency and power transmission capability.

The transmission efficiencies by using different strategies with respect to the output voltages when V_1=50V and P=150W are shown in Fig. 15(b). It illustrates that the measured transmission efficiencies of all control methods are firstly decreasing along with decreasing output voltage v_2. When the output voltage v_2 is changing from 50V to 30V, the efficiency

of SPS and EPS1 has dropped nearly 3% while the efficiencies of EPS2, MBC and GOM control has dropped 2.7%, 2%, and 2%, respectively. Since the power transmission capability is significantly limited under the high voltage conversion ratio conditions, FOPS cannot reach the condition of "P=150W" when the output voltage is below 45V. MBC, GOM and POPS control can ensure the higher transmission efficiency than SPS, EPS1, and EPS2 control under all voltage conversation conditions especially in the higher voltage conversation situations.

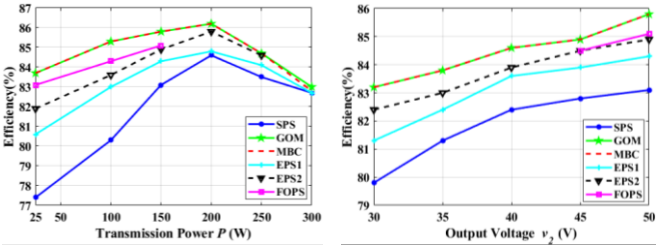

(a) (b)

Fig. 15. (a) Comparison of DAB operation efficiency varied with transmission power P when V_1=50V, nv_2=50V. (b) Comparison of DAB operation efficiency varied with output voltage v_2 when V_1=50V, P=150W.

F. Execution Time and Power Transmission Range Evaluation

An experimental comparison of DAB converters with SPS, FOPS, GOM, and MBC controls in terms of the execution time in the DSP TMS320F28335 and the power transmission range is shown in Table II.

TABLE II
EXPERIMENTAL COMPARISON OF DIFFERENT STRATEGIES IN TERMS OF THE EXECUTION TIME IN THE DSP TMS320F28335 CONTROLLER AND THE POWER TRANSMISSION RANGE

Control	Time (Cycle)	Time (ms)	Power (W)
SPS Control	468	0.003	0~320
FOPS Control	532	0.003	0~160
GOM Control	921	0.006	0~320
MBC Control	1432	0.009	0~320
MBC Control (Single NSS)	376	0.003	0~320

The measured execution time with SPS and FOPS control is 0.003ms, while the corresponding time with GOM and MBC control is 0.006ms and 0.009ms, respectively. Here, it is worth noticing that the measured execution time for the conventional NSS control, which is regarded as one special MBC state, is only 0.003ms. For the general MBC control, considering that it actually covers four NSS states, the practical execution time is found increased. In terms of the power transmission range, the proposed MBC control exhibits the same range as the SPS and GOM control, while the FOPS control shows half of the power transmission capability of other methods shown in Table II.

VII. CONCLUSION

In this paper, a minimum-current-stress boundary control by using the multiple-phase-shift based switching surfaces is proposed. Based on the mathematical models of multiple natural switching surfaces (NSS) and the LMM-based current stress optimization algorithm, the proposed MBC control can improve the steady-state efficiency and achieve fast dynamic response simultaneously for different conditions, including the startup, sudden voltage reference and load changing conditions. Both simulation and the experimental results are provided to validate the effectiveness of the proposed MBC algorithm. The research shows that the proposed control can achieve 8 times faster dynamic performance, less oscillations, eliminated dc-bias current, and higher steady-state efficiency for different power range. Although the execution time of the proposed MBC control is increased due to multiple NSS states covered within each switching cycle, the MBC control can be easily implemented by the off-the-shelf controllers or devices for high-frequency power converter applications.

REFERENCES

[1] B. Zhao, Q. Song, W. Liu, and Y. Sun, "Overview of Dual-Active-Bridge Isolated Bidirectional DC-DC Converter for High-Frequency-Link Power-Conversion System," *IEEE Transactions on Power Electronics*, vol. 29, pp. 4091-4106, 2014.

[2] C. Mi, H. Bai, C. Wang, and S. Gargies, "Operation, design and control of dual H-bridge-based isolated bidirectional DC–DC converter," *IET Power Electronics*, vol. 1, no. 4, p. 507, 2008.

[3] M. N. Kheraluwala, R. W. Gascoigne, D. M. Divan and E. D. Baumann, "Performance characterization of a high-power dual active bridge DC-to-DC converter," *IEEE Transactions on Industry Applications*, vol. 28, no. 6, pp. 1294-1301, Nov.-Dec. 1992.

[4] Y. Xie, J. Sun and J. S. Freudenberg, "Power Flow Characterization of a Bidirectional Galvanically Isolated High-Power DC/DC Converter Over a Wide Operating Range," *IEEE Transactions on Power Electronics*, vol. 25, no. 1, pp. 54-66, Jan. 2010.

[5] H. Zhou and A. M. Khambadkone, "Hybrid Modulation for Dual-Active-Bridge Bidirectional Converter With Extended Power Range for Ultracapacitor Application," *IEEE Transactions on Industry Applications*, vol. 45, no. 4, pp. 1434-1442, July-aug. 2009.

[6] Z. Guo and D. Sha, "Dual-Active-Bridge Converter With Parallel-Connected Full Bridges in Low-Voltage Side for ZVS by Using Auxiliary Coupling Inductor," *IEEE Transactions on Industrial Electronics*, vol. 66, no. 9, pp. 6856-6866, Sept. 2019.

[7] B. Zhao, Q. Yu, and W. Sun, "Extended-Phase-Shift Control of Isolated Bidirectional DC-DC Converter for Power Distribution in Microgrid," *IEEE Transactions on Power Electronics*, vol. 27, no. 11, pp. 4667-4680, 2012.

[8] H. Wen, W. Xiao, and B. Su, "Nonactive Power Loss Minimization in a Bidirectional Isolated DC-DC Converter for Distributed Power Systems," *IEEE Transactions on Industrial Electronics*, vol. 61, pp. 6822-6831, 2014.

[9] G. G. Oggier, G. O. GarcÍa and A. R. Oliva, "Switching Control Strategy to Minimize Dual Active Bridge Converter Losses," in *IEEE Transactions on Power Electronics*, vol. 24, no. 7, pp. 1826-1838, July 2009.

[10] A. Tong, L. Hang, g. li, x. jiang and S. Gao, "Modeling and Analysis of Dual-Active-Bridge Isolated Bidirectional DC/DC Converter to Minimize RMS Current," *IEEE Transactions on Power Electronics*, in press.

[11] N. Hou, W. Song, and w. m, "Minimum-Current-Stress Scheme of Dual Active Bridge DC-DC Converter With Unified-phase-shift Control," *IEEE Transactions on Power Electronics*, vol. 31, no. 12, pp. 8552-8561, 2016.

[12] Segaran, D, Holmes, D.G, McGrath, B.P, "Enhanced Load Step Response for a Bidirectional DC-DC Converter," *IEEE Transactions on Power Electronics*, vol.28, no. 1, pp. 371-379, 2013.

[13] F. Xiong, J. Wu, Z. Liu and L. Hao, "Current Sensorless Control for Dual Active Bridge DC–DC Converter with Estimated Load-Current Feedforward," *IEEE Transactions on Power Electronics*, vol. 33, no. 4, pp. 3552-3566, April 2018.

[14] H. Qin, K. J.W, and w. m, "Closed-Loop Control of DC-DC Dual-Active-Bridge Converter Driving Single-Phase Inverters," *IEEE Transactions on Power Electronics*, vol. 29, no. 2, pp. 1006-1017, 2014.

[15] A. R. Oliva, S. S. Ang, and G. E. Bortolotto, "Digital control of a voltage mode synchronous buck converter," *IEEE Trans. Power Electron.*, vol. 21, no. 1, pp. 175–163, Dec. 2006.

[16] H. Qin and J. W. Kimball, "Closed-Loop Control of DC–DC Dual-Active-Bridge Converters Driving Single-Phase Inverters," *IEEE Transactions on Power Electronics*, vol. 29, no. 2, pp. 1006-1017, Feb. 2014.

[17] Y. Jeung and D. Lee, "Voltage and Current Regulations of Bidirectional Isolated Dual-Active-Bridge DC–DC Converters Based on a Double-Integral Sliding Mode Control," *IEEE Transactions on Power Electronics*, vol. 34, no. 7, pp. 6937-6946, July 2019.

[18] O. M. Hebala, A. A. Aboushady, K. H. Ahmed and I. Abdelsalam, "Generic Closed-Loop Controller for Power Regulation in Dual Active Bridge DC–DC Converter With Current Stress Minimization," *IEEE*

Transactions on Industrial Electronics, vol. 66, no. 6, pp. 4468-4478, June 2019.B. Zhao, Q. Song, W. Liu and Y. Zhao, "Transient DC Bias and Current Impact Effects of High-Frequency-Isolated Bidirectional DC–DC Converter in Practice," *IEEE Transactions on Power Electronics*, vol. 31, no. 4, pp. 3203-3216, April 2016.

[19] X. Li and Y. Li, "An Optimized Phase-Shift Modulation For Fast Transient Response in a Dual-Active-Bridge Converter," *IEEE Transactions on Power Electronics*, vol. 29, no. 6, pp. 2661-2665, June 2014.

[20] Q. Bu, H. Wen, J. Wen, Y. Hu and Y. Du, "Transient DC Bias Elimination of Dual Active Bridge DC-DC Converter with Improved Triple-Phase-Shift Control," *IEEE Transactions on Industrial Electronics*, Early Access

[21] B. Zhao, Q. Song, W. Liu and Y. Zhao, "Transient DC Bias and Current Impact Effects of High-Frequency-Isolated Bidirectional DC–DC Converter in Practice," *IEEE Transactions on Power Electronics*, vol. 31, no. 4, pp. 3203-3216, April 2016.

[22] M. Anun, M. Ordonez, I. G. Zurbriggen and G. G. Oggier, "Circular Switching Surface Technique: High-Performance Constant Power Load Stabilization for Electric Vehicle Systems," *IEEE Transactions on Power Electronics*, vol. 30, no. 8, pp. 4560-4572, Aug. 2015.

[23] G. G. Oggier, M. Ordonez, J. M. Galvez, and F. Luchino, "Fast transient boundary control and steady-state operation of the dual active bridge converter using the natural switching surface," *IEEE Trans. Power Electron.*, vol. 29, no. 2, pp. 946–957, Feb. 2014.

[24] G. G. Oggier and M. Ordonez, "Boundary Control of Full-Bridge ZVS: Natural Switching Surface for Transient and Steady-State Operation," *IEEE Transactions on Industrial Electronics*, vol. 61, no. 2, pp. 969-979, Feb. 2014.

[25] G. G. Oggier and M. Ordonez, "High-Efficiency DAB Converter Using Switching Sequences and Burst Mode," *IEEE Transactions on Power Electronics*, vol. 31, no. 3, pp. 2069-2082, March 2016.

[26] S. Shao, M. Jiang, W. Ye, Y. Li, J. Zhang and K. Sheng, "Optimal Phase-Shift Control to Minimize Reactive Power for a Dual Active Bridge DC–DC Converter," *IEEE Transactions on Power Electronics*, vol. 34, no. 10, pp. 10193-10205, Oct. 2019.

[27] A. K. Bhattacharjee and I. Batarseh, "Optimum Hybrid Modulation for Improvement of Efficiency Over Wide Operating Range for Triple-Phase-Shift Dual-Active-Bridge Converter," IEEE Transactions on Power Electronics, vol. 35, no. 5, pp. 4804-4818, May 2020.

[28] B. Zhao, Q. Song, W. Liu, G. Liu, and Y. Zhao, "Universal High-Frequency-Link Characterization and Practical Fundamental-Optimal Strategy for Dual-Active-Bridge DC-DC Converter Under PWM Plus Phase-Shift Control," *IEEE Transactions on Power Electronics*, vol. 30, pp. 6488-6494, 2015.

Haochen Shi was born in Hubei, China, in 1992. He received the B.S. degree from the Department of Electrical Engineering, China Three Gorge University, Yichang, China, in 2014. He received the M.Eng. degree from the Department of Electrical Engineering, University of Leicester, Leicester, UK, in 2015. He is currently working toward the Ph.D. degree at the University of Liverpool, U.K. His current research interests include bidirectional dc-dc converter, electrical vehicles, and renewable power conversion system.

Huiqing Wen (M'13) received his B.S. and M.S. degrees in Electrical Engineering from Zhejiang University, Hangzhou, China, in 2002 and 2006, respectively; and his Ph.D. degree in Electrical Engineering from the Chinese Academy of Sciences, Beijing, China, in 2009. From 2009 to 2010, he was an Electrical Engineer working in the Research and Development Center, GE (China) Co., Ltd., Shanghai, China. From 2010 to 2011, he was an Engineer at the China Coal Research Institute, Beijing, China. From 2011 to 2012, he was a Postdoctoral Fellow at the Masdar Institute of Science and Technology, Abu Dhabi, United Arab Emirates. Currently, he is presently working as an Associate Professor at the Xi'an Jiaotong-Liverpool University, Suzhou, China. His current research interests include bidirectional DC-DC converters, power electronics in flexible AC transmission applications, electrical vehicles, and high-power, three-level electrical driving systems.

Yihua Hu (M'13-SM'15) received his B.S. degree in Electrical Motor Drives, and his Ph.D. degree in Power Electronics and Drives, from the China University of Mining and Technology, Jiangsu, China, in 2003 and 2011, respectively. From 2011 to 2013, he was a Postdoctoral Fellow in the College of Electrical Engineering, Zhejiang University, Hangzhou, China. From November 2012 to February 2013, he was an Academic Visiting Scholar in the School of Electrical and Electronic Engineering, Newcastle University, Newcastle upon Tyne, ENG, UK. From 2013 to 2015, he worked as a Research Associate in the Power Electronics and Motor Drive Group, University of Strathclyde, Glasgow, SCT, UK. He is presently working as a Lecturer in the Department of Electrical Engineering and Electronics, University of Liverpool, Liverpool, ENG, UK. He has published more than 36 peer reviewed technical papers in leading journals. His current research interests include PV generation systems, power electronics converters and control, and electrical motor drives.